This MICCAI paper is the Open Access version, provided by the MICCAI Society. It is identical to the accepted version, except for the format and this watermark; the final published version is available on SpringerLink.

Two-Stage Generative Model for Intracranial Aneurysm Meshes with Morphological Marker Conditioning

Wenhao Ding[1[0000−0002−9665−7933]], Kangjun Ji[1[0009−0009−4152−6790]], Simão Castro[2[0009−0005−0967−951X]], Yihao Luo[1[0009−0002−1169−2930]], Dylan Roi[3[0000−0001−7775−9873]], and Choon Hwai Yap[1[0000−0003−2918−3077]*]

[1] Imperial College London, London SW7 2AZ, United Kingdom
*Corresponding author: c.yap@imperial.ac.uk
[2] Instituto Superior Técnico, Lisbon 1049-001, Portugal
[3] Imperial College Healthcare NHS Trust, London W6 8RF, United Kingdom

Abstract. A generative model for the mesh geometry of intracranial aneurysms (IA) is crucial for training networks to predict blood flow forces in real time, which is a key factor affecting disease progression. This need is necessitated by the absence of a large IA image datasets. Existing shape generation methods struggle to capture realistic IA features and ignore the relationship between IA pouches and parent vessels, limiting physiological realism and their generation cannot be controlled to have specific morphological measurements. We propose AneuG, a two-stage Variational Autoencoder (VAE)-based IA mesh generator. In the first stage, AneuG generates low-dimensional Graph Harmonic Deformation (GHD) tokens to encode and reconstruct aneurysm pouch shapes. GHD enables more accurate shape encoding than alternatives. In the second stage, AneuG generates parent vessels conditioned on GHD tokens, by generating vascular centerline and propagating the cross-section. IA shape generation can be conditioned on specific clinically relevant shape measurements, enabling controlled studies on how morphological variations impact flow behaviors. Additional, our novel Morphing Energy Alignment constraint and Morphological Marker Calculator improve generation fidelity and controllability. Source code and implementation details are available at https://github.com/anonymousaneug/AneuG.

Keywords: Intracranial Aneurysms · 3D Shape Generation.

1 Introduction

Intracranial aneurysm (IA) is a vascular disease where a weakness in the vascular wall causes a bulge, which carries risks of severe consequences if it ruptures. With advancements in imaging technology, IAs are increasingly detected, with a prevalence of up to 8% [1]. The prediction of rupture risk is currently difficult [2], but the IA morphological shape and the consequent pattern of blood fluid forces on the IA pouch are thought to influence it [3]. As such, it will be useful

to develop neural networks for rapid prediction of flow dynamics in IAs, for use in large clinical data testing of predictive power of fluid dynamics features, and if successful, for subsequent use as a clinical tool to predict rupture risks. To train such a network [4], a large dataset of morphologies is necessary, but this is not readily available, necessitating shape generation.

Unfortunately, existing models for synthesizing IA geometries are not yet robust. First, they do not model the joint distribution of IAs and their parent vessel geometries. Instead, they either adopt idealized vessels to merge with generated IA pouches [6] or merge real IAs to healthy parent vessels from other individuals [7]. Secondly, some models generate IA pouches via manual deformations [8], but this is not data-driven and results may be unrealistic.

Third, the ability to control the generated IA geometries to achieve specific clinical morphological parameters remains an unmet need. Such controls will allow us to generate shape cohorts with clinically relevant statistics, and understand shape variability within specific clinical measurements. It will also enable the generation of realistic geometries that vary only in specific shape features while keeping all other features constant, which would be invaluable for studies aimed at understanding the effects of individual morphological features on IA fluid mechanics. Current generation models have not achieved this. Past works have been limited to selecting shapes from cohorts in an uncontrolled manner [9,10,11] or relying on non-physiological synthetic shapes [6,12].

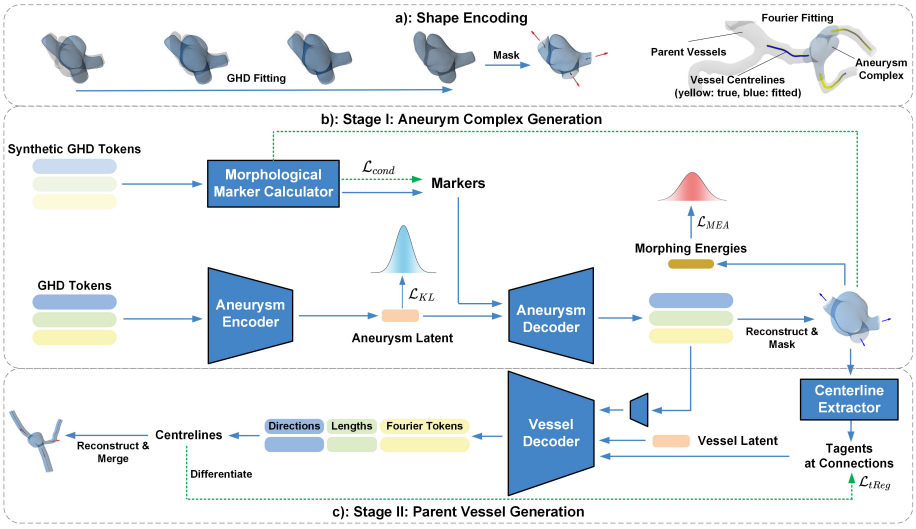

Fig. 1. Overview of AneuG.

To address these unmet needs, we propose a two-stage conditional generation model, AneuG. In the first stage, the model generates the IA pouch and regions

immediately surrounding it — referred to as the aneurysm complex—conditional to having specific values for certain clinically relevant morphological parameters. In the second stage, the parent vessels are generated, conditional to features of the generated aneurysm complex. Both stages employ shape encoding and approximate the latent distributions using a Variational Autoencoder (VAE). This enables accurate reconstruction of 3D shapes with a relatively small dataset, which is challenging for mainstream diffusion-based shape generators [15].

Our main contributions are: (1). We introduce AneuG, the first deep generative model for 3D IA meshes that simultaneously models the aneurysm complex and its parent vessels (that are sufficiently long for fluid mechanics investigations), with the latter conditioned on the former to ensure anatomical realism. (2). AneuG enables shape generation to specific clinically relevant morphological parameters via training with a differentiable Morphological Marker Calculator (MMC), allowing downstream controlled studies of how morphology affects hemodynamics. (3). We leverage Graph Harmonic Deformation (GHD) for shape encoding, capturing detailed local shape features. (4). We propose a Morphing Energy Alignment (MEA) constraint to enhance the generation fidelity. This is particularly necessary for conditional generation where fidelity becomes weaker.

2 Methods

2.1 Problem Statement and Overview

The schematic of our method is shown in Fig. 1. We aim to generate synthetic aneurysm meshes conditioned on specific values of certain clinical morphological markers $\boldsymbol{\lambda}$, supervised by a cohort of aneurysm shapes reconstructed from MRI. This process is accomplished with a two-stage VAE architecture.

In the first stage, the aneurysm complex undergoes shape feature encoding, in the form of GHD tokens, through a morphing process (see Section 2.2). Shapes generated by the unconditional VAE are used to estimate distributions of morphological parameters, which are then used for conditional generation. This ensures a physiologically realistic decoder that understands the conditional probability distributions when multiple parameters are involved. During training, a differentiable Morphological Marker Calculator (MMC) is used to compute the MSE loss, $\mathcal{L}_{\text{cond}}$, to ensure specified morphology parameters match generated ones. Additionally, we calculate the morphing energies of reconstructed shapes and align their distribution with that of real shapes (see Section 2.3).

In the second stage, we generate the centerlines of parent vessels conditioned on the aneurysm complex shape. Similar to stage one, we encode shape features, this time with Fourier tokens. To ensure IA pouch to vessel shape continuity, we compute the tangent vectors of the generated centerlines and constrain them to match that of vascular stubs on the aneurysm complex (red arrows in Fig. 1 **a)**) via $\mathcal{L}_{tReg}$, the MSE between the two. Finally, we propagate nodes of the connection cross-sections along the generated centerlines and merge them with the aneurysm complex to obtain the final mesh. For the merging, vascular stubs

on the stage I IA complex are first clipped, and the resulting cross-sections are propagated along the stage II centerline, with algorithmic insertion of additional triangle elements at the interface. Further details are provided in the codes.

2.2 Shape Encoding

We encode the 3D aneurysm shapes and their parent vessels before feeding them into VAEs. For the aneurysm complex, we apply the Graph Harmonic Deformation (GHD) method (surface Fourier basis), as it offers smoothness without regularization and can better capture local geometry than coordinate-based morphing or PCA [16]. A set of scalar tuples $\phi_i = (\phi_{ix}, \phi_{iy}, \phi_{iz})$, refered to as GHD tokens, can be found by morphing a canonical mesh $\mathcal{M}^c$ (defined by nodes $\mathcal{V}_c$ and faces $\mathcal{F}_c$) into a target mesh $\mathcal{M}^t$ through gradient descent (see Fig. 1 **a**):

$$\boldsymbol{\phi} = \arg\min_{\boldsymbol{\phi}} \mathcal{L}_{GHD}\left[\mathcal{M}\left(\mathcal{V} = \sum_{i=1}^{n} U_i \cdot \phi_i, \mathcal{F}_c\right), \mathcal{M}^t\right] \tag{1}$$

where $\mathcal{V}_c$ and $\mathcal{F}_c$ denote the mesh node coordinates and triangle faces of the canonical shape. U_i is the ith eigenvector of the canonical mesh's cotangent graph Laplacian. We truncate the number of eigenvector modes to a small number n. $\mathcal{L}_{GHD}$ is the loss function evaluating the distance between the warped canonical mesh and the target mesh. We follow the design in [16] and add additional Chamfer Distance constraints on vessel cross-sections to guide the morphing process. Further details are in the GHD citation [16].

For the parent vessels, we encode their centerlines in a similar way. We model the vessel branches as warped beams constructed with sine functions shape modes, ψ, and corresponding amplitudes, φ [23]. The centerline function of parent vessels in the global coordinate system is therefore expressed as:

$$L_k = \mathbf{R_k}(\mathbf{v}_k) \cdot \left[\tilde{x}_k, \tilde{y}_k = \textstyle\sum_i \varphi_i \cdot \psi_{ik}, \tilde{z}_k = \sum_j \varphi_j \cdot \psi_{jk}\right]^T + \mathbf{c}_k \tag{2}$$

$$\psi_i(\tilde{x}_k) = \sin(i\pi/l_k * \tilde{x}_k),\ \tilde{x} \in [0, l_k] \tag{3}$$

where k represents the branch index, i and j are beam mode indices, and l_k the unwarped beam length. $\mathbf{v}_k$ is the normalized direction vector of the branch (from start to end) that parameterizes the rotation matrix $\mathbf{R_k}$ from the local to global coordinate system. The transition $\mathbf{c}_k$ is equal to the coordinate of the vessel cross-section center. An example of a fitted case is visualized in Fig. 1 **a**.

2.3 Stage I training

We train a VAE to model the distribution of GHD tokens $\boldsymbol{\phi}$. Synthetic aneurysm complex meshes $\mathcal{M}^\alpha$ are conditionally reconstructed with $\boldsymbol{\phi}$ sampled from the approximated posterior distribution $q_\theta^\alpha(\boldsymbol{\phi} \mid \boldsymbol{z}, \boldsymbol{\lambda})$:

$$\mathcal{M}^\alpha = \mathcal{M}\left(\mathcal{V} = \sum_{i=1}^{n} U_i \cdot \phi_i, \mathcal{F}_c\right) \tag{4}$$

The reconstruction loss term consists of the MSE loss of GHD tokens and the Chamfer Distances between the real and reconstructed shapes.

Morphing Energy Alignment: To mitigate the limitations of a small training dataset, we incorporate additional information into the VAE training process. Our hypothesis is that generated shapes, if they closely resemble real shapes, should exhibit a similar population distribution of morphing energies (from canonical to target mesh) as the real shapes. In this work, we utilize rigidity energy E_r as defined in [17] and Laplacian smoothness E_l as described in [18]. Shapiro–Wilk tests conducted on our training dataset reveal that both energy distributions are normal. Based on this observation, we sample from the encoded distribution of real shapes during training and generate corresponding synthetic shapes, compute their morphing energies, and align their distributions with those of the real shapes through KL divergence:

$$\mathcal{L}_{MEA} = \sum_i D_{\mathrm{KL}} \left(\mathcal{N}(\mu_i^{\mathrm{real}}, (\sigma_i^{\mathrm{real}})^2) \parallel \mathcal{N}(\mu_i^{\mathrm{syn}}, (\sigma_i^{\mathrm{syn}})^2) \right) \tag{5}$$

where μ and σ^2 are population mean and variance of morphing energies ($i \in \{E_r, E_l\}$) computed on real / synthetic shapes.

Morphological Marker Calculator (MMC): Leveraging on the mesh-preserving nature of GHD, our method enables consistent registration between different aneurysm complexes. This allows easy differentiable calculation of morphological markers from the mesh. Markers calculated include neck width (NW), aspect ratio (AR), and a novel lobulation index (LI)—defined as dome surface area divided by volume. Dome volume is further computed by closing the mesh and applying the discrete Gaussian theorem. We use the MMC to estimate the multivariate distribution of morphological conditions from synthetic shapes generated by an unconditional stage-I VAE. This avoids unrealistic combinations like concurrently high AR and NW.

2.4 Stage II training

We train another VAE to generate parent vessels. Synthetic centerlines are reconstructed through sampling from the distribution of Fourier mode coefficients $\boldsymbol{\varphi}$ defined in Eq. (2), the direction vector of the vessel branch $\boldsymbol{v}$ (with respect to the tangent vector t_c at the vessel cross-section), and the branch length l:

$$q_\theta^\beta(\{\boldsymbol{\varphi}, \boldsymbol{v}, \boldsymbol{l}\} \mid \boldsymbol{z}, \boldsymbol{\phi}) \tag{6}$$

where the decoder inputs are the parameterized IA complex generated in stage I (condition) and vessel latent representation, $\boldsymbol{\phi}$ and z, respectively. We then propagate the cross sections of the aneurysm complex along the synthetic centerlines to create tubular meshes and merge them with the masked aneurysm complex mesh to obtain the final mesh. The reconstruction loss consists of MSE losses on tokens and centerlines points. We also conduct spatial differentiation of the reconstructed centerlines and force their tangent directions at the connections to the aneurysm complex to match t_c.

Table 1. Evaluation of unconditional generation. ↑: larger value is better; ↓: vice versa. **Bold** metrics: best performance among methods. *****: Trained with MEA. CD_v is shown in 10^{-4}, while CD_n is shown in 10^{-2}.

Model	FPD↓	KPD↓	TMD↑	$CD_v \downarrow$	$CD_n \downarrow$
AneuG*	$\mathbf{6.06 \pm 0.34}$	$\mathbf{1.10 \pm 0.12}$	5.89 ± 0.09	$\mathbf{1.88 \pm 0.08}$	3.63 ± 0.08
AneuG	8.22 ± 1.01	2.32 ± 0.42	4.90 ± 0.16	1.95 ± 0.10	$\mathbf{3.53 \pm 0.16}$
PCA	13.52 ± 0.15	7.78 ± 0.54	6.45 ± 0.21	88.33 ± 2.21	52.87 ± 0.64
Diffusion	45.18 ± 1.71	62.33 ± 5.23	$\mathbf{25.48 \pm 1.95}$	10.93 ± 0.31	124.57 ± 0.19

3 Experiments

Dataset. We use the the largest publicly available IA dataset, AneuX, to evaluate our model. As we are focussing on IA located at the middle cerebral artery bifurcation in this work, we extracted 116 IAs within AneurX of this nature for training. Ground truth vascular centerlines were extracted with VMTK.

Metrics. Following [13], we adopt Fréchet PointNet++ Distance (FPD) and Kernel PointNet++ Distance (KPD) using a pre-trained PointNet++ to evaluate fidelity of generated latent space distribution. We follow [20] and use Total Mutual Difference (TMD) to evaluate the diversity. For VAE reconstruction evaluation, we use Chamfer Distance on mesh nodes (CD_v) and face normals (CD_n). CD_v and TMD are measured in mm^2, other metrics are unitless. For conditioning accuracy (CA), We use the relative L2 error on recalled conditions.

Unconditional Shape Generation Performance. Unconditional generation results are presented in Table 1. We compared our AneuG to a generator based on a node-wise Principal Component Analysis (PCA) statistical shape model (using 15 modes) [14], which is a prevailing biomedical shape model in the literature, and a deep learning Diffusion shape generator. The Diffusion model is composed of a VAE trained on the occupancy field of aneurysm complexes and a transformer UNet-based latent diffusion network [15], but is without image/text conditioning. Further details can be found in our codes. The results indicate that AneuG achieves superior generation fidelity and reconstruction accuracy relative to baseline methods. Results are visualized in Fig. 2 **a-b**, where it is observed that AneuG produces smooth and refined surface meshes, even with only 116 training data, whereas the diffusion model fails to achieve comparable quality. We also observe that PCA achieves smooth generation but fails to capture local features on the aneurysm pouches. These results justify the use of GHD in our approach, which enables AneuG to capture more local features. We further requested a neuroradiologist rank the shape generations from competing models on how realistic they look. AneuG with MEA ranked highest, while AneuG without MEA ranked highest in diversity.

Ablation studies of MEA and MMC. Conditional generation experiments are conducted to quantify the contributions of MEA and MMC. While Table 1 indicates that MEA provides only a marginal improvement in generation fidelity in the unconditional scenario, its impact is more substantial in conditional settings. The performance gap across condition setups in Table 2

Table 2. Conditional generation evaluation. **AR**: Aspect ratio. **NW**: Neck width. **LI**: Lobulation index. **V**: Dome volume. **Bold** metrics: best performance for each setup. *****: Trained with MEA. †: Trained with MMC. Other details as per Table 1.

Condition	FPD↓	KPD↓	TMD↑	CA(%)↓	$CD_v \downarrow$	$CD_n \downarrow$
AR	14.88 ± 0.76	11.21 ± 0.38	3.83 ± 0.03	8.72 ± 0.23	2.79	4.02
AR*	9.54 ± 0.27	4.28 ± 0.31	4.39 ± 0.13	9.30 ± 0.40	**1.73**	**3.51**
AR*†	$\mathbf{7.86 \pm 0.49}$	$\mathbf{2.78 \pm 0.07}$	$\mathbf{4.56 \pm 0.10}$	$\mathbf{2.93 \pm 0.14}$	2.11	3.89
NW	12.41 ± 0.70	9.27 ± 0.88	4.10 ± 0.13	3.35 ± 0.17	2.61	**3.45**
NW*	10.50 ± 0.46	4.66 ± 0.21	$\mathbf{4.43 \pm 0.12}$	3.68 ± 0.04	**1.95**	3.48
NW*†	$\mathbf{8.48 \pm 0.23}$	$\mathbf{4.07 \pm 0.46}$	4.47 ± 0.01	$\mathbf{1.80 \pm 0.04}$	3.95	3.69
AR+NW	12.56 ± 0.80	8.35 ± 0.66	4.44 ± 0.03	5.88 ± 0.28	2.97	4.40
AR+NW*	11.13 ± 0.95	5.48 ± 0.30	4.27 ± 0.16	6.93 ± 0.59	2.71	5.12
AR+NW*†	$\mathbf{10.24 \pm 0.44}$	$\mathbf{4.22 \pm 0.32}$	$\mathbf{4.06 \pm 0.07}$	$\mathbf{2.78 \pm 0.18}$	**2.06**	**4.27**
LI	17.94 ± 0.60	21.68 ± 0.68	3.75 ± 0.11	11.49 ± 0.60	17.18	20.56
LI+V*	$\mathbf{13.20 \pm 0.36}$	$\mathbf{6.79 \pm 0.58}$	4.01 ± 0.11	12.91 ± 0.52	4.68	8.60
LI+V*†	15.16 ± 0.65	9.22 ± 0.52	$\mathbf{3.13 \pm 0.16}$	$\mathbf{3.19 \pm 0.29}$	**4.52**	**8.18**

can be attributed to limited data. With limited samples, using more conditions makes the training harder. Table 2 demonstrates that incorporating MEA consistently enhances generation fidelity under all condition configurations. This improvement can be attributed to MEA mitigating posterior collapse during conditional training in the first stage, which otherwise reduces the preservation of shape structures and leads to a misaligned morphing energy distribution. By ensuring alignment of the morphing energy distribution with the dataset, MEA helps AneuG maintain more structural details. MMC demonstrates increased conditioning accuracy across all experimental configurations, with a minor improvement in generation fidelity observed in most cases. However, using MEA and MMC increases training time from ∼1 h to ∼4 h on one RTX 3090 GPU. (Up to 5 concurrent runs can be performed within the same training time.)

Application. By encoding a real shape and fixing the latent code while varying the condition variable, we can morph it to varying morphological parameters. In Fig. 2 **e**, we demonstrate that increasing AR incrementally results in a higher aneurysm dome. In Fig. 2 **f**, we show that by holding the volume of the real shape constant, but increasing lobulation index, a daughter sac can be created, which is a marker of IA rupture risk [2]. Additionally, Fig. 2**g** shows the model's ability to generate long vascular inlets and outlets, which is necessary for downstream biofluid mechanics simulation studies as they strongly influence fluid dynamics. We performed flow simulations using Ansys Fluent [22] and found that higher IA aspect ratio (AR) causes increased areas of low wall shear stress (WSS), while the presence of a daughter sac causes more complex and chaotic flow. This corroborates prevailing thinking: these flow features are considered mechanical stimuli that can cause adverse biological responses [3], while these morphology features are understood to be markers for disease progression and rupture risks [21]. Our simulation results also align with clinical observations linking large AR to higher rupture risk, as increased low-WSS regions appear

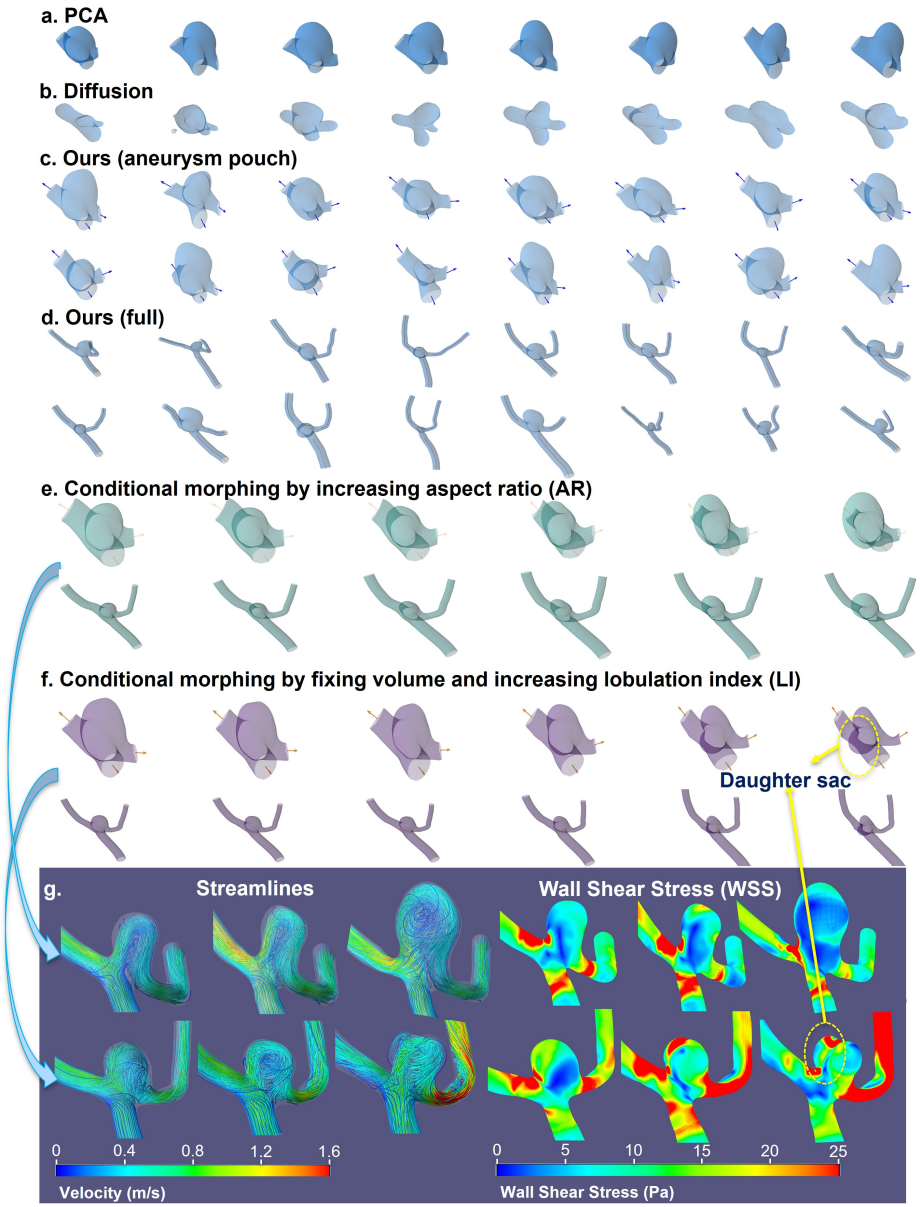

Fig. 2. Generation gallery. Rotational video for **c** and **d** are provided in supplementary material.

on the aneurysm pouch (generally considered dangerous) [3]. These applications show how AneuG's conditional morphing enables future larger scale studies to better understanding how IA biomechanics influence rupture risk.

4 Conclusion

In this paper, we propose a conditional generation model for intracranial aneurysms. The model captures the joint distribution of aneurysm complexes and their parent vessels, providing a novel solution to this field. The proposed method outperforms the main-stream diffusion model with limited data and therefore highlights its applicability to rare cerebral aneurysm complexes. However, several limitations remain. First, the dataset used for training is relatively small, limiting the diversity and fidelity of generated shapes, particularly under strict morphological conditioning. Second, only bifurcation-type IAs are included. Third, human evaluations were based on a single neuroradiologist, a larger panel of reviewers will strengthen confidence of the visual realism evaluation. Future work to address these limitations is warranted. Other future research direction include temporal conditioning with longitudinal data to model disease progression and leveraging the shape knowledge in AneuG to synthesize images.

Disclosure of Interests. The authors declare no competing interests.

References

1. Lee, K.S., Zhang, J.J.Y., Nguyen, V., Han, J., Johnson, J.N., Kirollos, R., Teo, M.: The Evolution of Intracranial Aneurysm Treatment Techniques and Future Directions. Neurosurgical Review **45**(1), 1–25 (2022).
2. Mocco, J., Brown, R.D., Torner, J.C., Capuano, A.W., Fargen, K.M., Raghavan, M.L., Piepgras, D.G., Meissner, I., Huston, J.: Aneurysm Morphology and Prediction of Rupture: An International Study of Unruptured Intracranial Aneurysms Analysis. Neurosurgery **82**(4), 491–496 (2018).
3. Zhou, G., Zhu, Y., Yin, Y., Su, M., Li, M.: Association of Wall Shear Stress with Intracranial Aneurysm Rupture: Systematic Review and Meta-Analysis. Scientific Reports **7**(1), 5331 (2017). doi: 10.1038/s41598-017-05886-w. Erratum in: Scientific Reports **8**(1), 5244 (2018).
4. Li, G., Wang, H., Zhang, M. et al.: Prediction of 3D Cardiovascular Hemodynamics Before and After Coronary Artery Bypass Surgery via Deep Learning. Communications Biology **4**, 99 (2021).
5. Merritt, W.C., Berns, H.F., Ducruet, A.F., Becker, T.A.: Definitions of intracranial aneurysm size and morphology: A call for standardization. Surgical Neurology International **12**, 506 (2021).
6. Goetz, A., Jeken-Rico, P., Pelissier, U., Chau, Y., Sédat, J., Hachem, E.: AnXplore: a comprehensive fluid-structure interaction study of 101 intracranial aneurysms. Frontiers in Bioengineering and Biotechnology **12** (2024).
7. Nader, R., Autrusseau, F.: Building a Synthetic Vascular Model: Evaluation in an Intracranial Aneurysms Detection Scenario. arXiv preprint arXiv:2411.02477 (2024)

8. Li, X., Zhou, Y., Xiao, F., Guo, X., Zhang, Y., Jiang, C., Ge, J., Wang, X., Wang, Q., Zhang, T., Lin, C., Cheng, Y., Qi, Y.: Aneumo: A Large-Scale Comprehensive Synthetic Dataset of Aneurysm Hemodynamics. arXiv preprint arXiv:2501.09980 (2025).
9. Lv, N., Karmonik, C., Chen, S. et al.: Wall Enhancement, Hemodynamics, and Morphology in Unruptured Intracranial Aneurysms with High Rupture Risk. Translational Stroke Research **11**, 882–889 (2020).
10. Qiu, T., Jin, G., Xing, H. et al.: Association between hemodynamics, morphology, and rupture risk of intracranial aneurysms: a computational fluid modeling study. Neurological Sciences **38**, 1009–1018 (2017).
11. Schnell, S., Ansari, S.A., Vakil, P., Wasielewski, M., Carr, M.L., Hurley, M.C., Bendok, B.R., Batjer, H., Carroll, T.J., Carr, J., Markl, M.: Three-dimensional hemodynamics in intracranial aneurysms: influence of size and morphology. Journal of Magnetic Resonance Imaging **39**(1), 120–131 (2014).
12. Li, G., Song, X., Wang, H., Liu, S., Ji, J., Guo, Y., Qiao, A., Liu, Y., Wang, X.: Prediction of Cerebral Aneurysm Hemodynamics With Porous-Medium Models of Flow-Diverting Stents via Deep Learning. Frontiers in Physiology **12**, 733444 (2021).
13. Zhang, B., Tang, J., Niessner, M., Wonka, P.: 3DShape2VecSet: A 3D Shape Representation for Neural Fields and Generative Diffusion Models. arXiv preprint arXiv:2301.11445 (2023).
14. Catalano, C., Agnese, V., Gentile, G., Raffa, G.M., Pilato, M., Pasta, S.: Atlas-Based Evaluation of Hemodynamic in Ascending Thoracic Aortic Aneurysms. Applied Sciences **12**(1), 394 (2022).
15. Zhao, Z., Liu, W., Chen, X., Zeng, X., Wang, R., Cheng, P., Fu, B., Chen, T., Yu, G., Gao, S.: Michelangelo: Conditional 3D Shape Generation based on Shape-Image-Text Aligned Latent Representation. In: Advances in Neural Information Processing Systems **36**, pp. 73969–73982. Curran Associates, Inc. (2023).
16. Luo, Y., Sesija, D., Wang, F., Wu, Y., Ding, W., Huang, J., et al.: Explicit Differentiable Slicing and Global Deformation for Cardiac Mesh Reconstruction. arXiv preprint arXiv:2409.02070v2 (2024).
17. Sorkine, O., Alexa, M.: As-Rigid-As-Possible Surface Modeling. In: Belyaev, A., Garland, M. (eds.) Geometry Processing, pp. 109–116. The Eurographics Association (2007).
18. Desbrun, M., Meyer, M., Schröder, P., Barr, A.H.: Implicit fairing of irregular meshes using diffusion and curvature flow. In: Proceedings of the 26th Annual Conference on Computer Graphics and Interactive Techniques (SIGGRAPH '99), pp. 317–324. ACM Press/Addison-Wesley Publishing Co. (1999).
19. Kipf, T.N., Welling, M.: Semi-Supervised Classification with Graph Convolutional Networks. arXiv preprint arXiv:1609.02907 (2017).
20. Zhou, L., Du, Y., Wu, J.: 3D Shape Generation and Completion Through Point-Voxel Diffusion. In: Proceedings of the IEEE/CVF International Conference on Computer Vision (ICCV), pp. 5826–5835. IEEE (2021).
21. Etminan, N., Brown, R.D., Jr., Beseoglu, K., et al.: The Unruptured Intracranial Aneurysm Treatment Score: A Multidisciplinary Consensus. Neurology **85**(10), 881–889 (2015).
22. Chan, W.X., Ding, W., Li, B., Wong, H.S., Yap, C.H.: Role of physics-informed constraints in real-time estimation of 3D vascular fluid dynamics using multi-case neural network. Computers in Biology and Medicine **190**, 110074 (2025).
23. Timoshenko, S.P., Young, D.H.: *Vibration Problems in Engineering*. D. Van Nostrand Company Inc. (1937).